Crystal growth and magnetic properties of the coupled alternating $S = 1$ spin chain $Sr_2Ni(SeO_3)_3$

R. Madhumathy,[1] K. Saranya,[1] K. Moovendaran,[2] K. Ramesh Babu,[3,4] Arpita Rana,[5] Kwang-Yong Choi,[6] Heung-Sik Kim,[7] Wei-Tin Chen,[8,9] M. Ponmurugan,[1] R. Sankar,[2,*] and I. Panneer Muthuselvam[5,†]

[1]*Department of Physics, School of Basic and Applied Sciences, Central University of Tamil Nadu, Neelakudi, Thiruvarur, 610005 Tamil Nadu, India*

[2]*Institute of Physics, Academia Sinica, Taipei 10617, Taiwan*

[3]*Department of Physics, National Taiwan University, Taipei 10617, Taiwan*

[4]*Physics Division, National Center for Theoretical Sciences, Hsinchu 30013, Taiwan*

[5]*Department of Physics (MMV), Banaras Hindu University, Varanasi, 221005 Uttar Pradesh, India*

[6]*Department of Physics, Sungkyunkwan University, Suwon 16419, Republic of Korea*

[7]*Department of Physics and Institute of Quantum Convergence Technology, Kangwon National University, Chuncheon 24311, Republic of Korea*

[8]*Center for Condensed Matter Sciences, National Taiwan University, Taipei 10617, Taiwan*

[9]*Taiwan Consortium of Emergent Crystalline Materials, Ministry of Science and Technology, Taipei 10622, Taiwan*

(Received 1 March 2023; revised 9 May 2023; accepted 17 May 2023; published 2 June 2023)

The structural, magnetic, and thermodynamic properties of a quasi-one-dimensional (1D) $S = 1$ alternating spin chain compound $Sr_2Ni(SeO_3)_3$ are investigated by using synchrotron x-ray powder diffraction, magnetic susceptibility $\chi(H, T)$, and heat capacity $C_P(H, T)$ measurements together with density functional theory (DFT) calculations. The $\chi(H, T)$ and $C_P(H, T)$ data reveal long-range antiferromagnetic order at $T_N = 3.4(3)$ K and short-range order at $T_m \approx 7.8$ K. The short-range magnetic order together with 95% of spin entropy release above T_N signifies the importance of 1D spin correlations persisting to $\sim 8T_N$. Theoretical DFT calculations with generalized gradient approximation determine leading exchange interactions, suggesting that interchain interactions are responsible for the observed long-range magnetic ordering. In addition, the temperature-field phase diagram of $Sr_2Ni(SeO_3)_3$ is determined based on the $\chi(T, H)$ and $C_P(T, H)$ data. Interestingly, a nonmonotonic phase boundary of T_m is found for an external field applied along a hard axis. Our results suggest that the ground state and magnetic behavior of $Sr_2Ni(SeO_3)_3$ rely on the interplay of single-ion anisotropy, bond alternation, and interchain interactions.

DOI: 10.1103/PhysRevB.107.214406

I. INTRODUCTION

Low-dimensional spin systems, such as one-dimensional (1D) chains, zigzag chains, and alternating chains, have been the subject of much attention in condensed matter physics due to their unique magnetic properties arising from pronounced quantum fluctuations and low dimensionality [1]. It is well established that 1D spin chains possess fundamentally different ground states between half-integer and integer spins.

Half-integer spin chains feature a gapless excitation spectrum and algebraically decaying correlations at $T = 0$ K. In the presence of interchain interactions, thus, the half-integer spin ground state is prone to long-range magnetic order [2,3]. In sharp contrast, integer spin chains have a cooperative singlet ground state with an excitation gap and short-range pair correlations [4–7]. The Haldane gap in integer spin chains protects the system against magnetic ordering. However, real materials are often subject to various perturbations, including single-ion anisotropy D, interchain interactions J', and bond alternation, which can modify the ground-state properties. For instance, anisotropy and bond alternation can create additional energy gaps, whereas interchain interactions can renormalize the Haldane gap and eventually induce long-range magnetic order. If J' is sufficiently strong, the Haldane gap can close, and a large-D gap can open at a critical point $D = 0.97J$, leading to two topologically distinct gapped phases [8]. On the other hand, bond alternation can also bring about a quantum phase transition from the Haldane to the dimer phase [9].

$Sr_2Ni(SeO_3)_3$ crystallizes in the triclinic space group $P\bar{1}$ with $a = 7.286(10)$ Å, $b = 7.581(2)$ Å, and $c = 8.722(2)$ Å [10]. The three-dimensional (3D) crystal structure of $Sr_2Ni(SeO_3)_3$, shown in Fig. 1(a), is composed of distorted NiO_6 octahedra [Fig. 1(b)], irregular 8-vertex SrO_8 polyhedra, and SeO_3 pyramids. There are no direct exchange interactions between Ni ($3d^8$) ions. From a structural point of view, the alternating chain along the c axis is formed by intrachain exchange interactions J_{i1} and J_{i2} [see Fig. 1(c)]. Here, J_{i1} is mediated through a corner-sharing network of SeO_3 pyramids, while J_{i2} involves Ni-O-Se-O-Ni and Ni-O-Sr-O-Ni super-superexchange paths. As sketched in Figs. 1(d) and 1(e), the five interchain exchange interactions J_{cj} ($j = 1$–5) are permitted along the a and b axes. Contrary to what is expected from

*sankarndf@gmail.com
†ipmphysics@gmail.com

 ©2023 American Physical Society

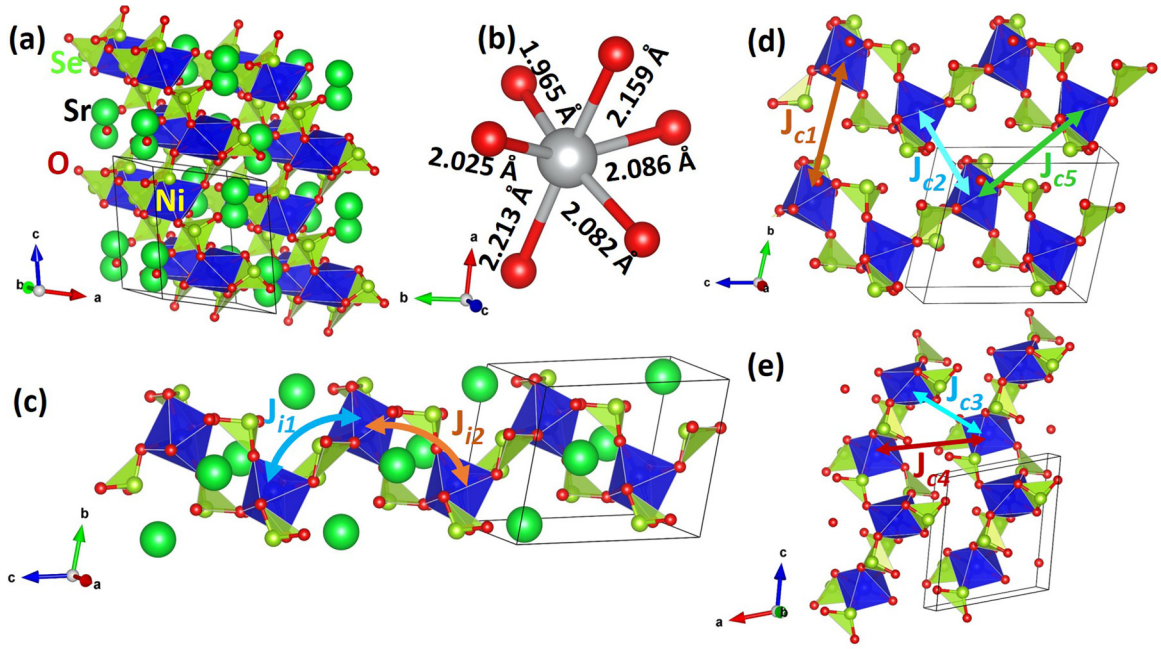

FIG. 1. (a) Schematic illustration of the three-dimensional crystal structure of $Sr_2Ni(SeO_3)_3$. (b) Distorted octahedra of NiO_6 with Ni-O distances. [(c)–(d)] and (e) Exchange interaction paths mediating Ni ions and their network connectivity.

the structure, our density functional theory (DFT) calculations reveal the $J_{i1}-J_{c3}$ alternating spin chain with small perturbative terms including J_{i2} and J_{cj} ($j = 1$–2 and 4–5) as discussed in Sec. III D.

Although the structure of the $Sr_2Ni(SeO_3)_3$ compound was reported a decade earlier [10], no detailed study of its physical properties has been made thus far. In this paper, we present a comprehensive investigation of the single-crystal growth, magnetic, electric, and thermodynamic behavior of single-crystal $Sr_2Ni(SeO_3)_3$ using a combination of diverse experimental techniques and DFT calculations. Based on the magnetic susceptibility $\chi(T, H)$ and specific heat $C_P(T, H)$ data, we evince short-range magnetic order at $T_m \sim 7.8$ K and a subsequent antiferromagnetic (AFM) transition at $T_N = 3.4$ K and draw the H-T phase diagram. Persistent magnetic correlations up to $\sim 8T_N$ and a nonmonotonic phase boundary of T_m suggest a complex interplay of single-ion anisotropy, bond alternation, and interchain interactions.

II. EXPERIMENTAL AND COMPUTATIONAL DETAILS

Single crystals of $Sr_2Ni(SeO_3)_3$ were grown using the hydrothermal technique. High-purity $Sr(OH)_2$, $Ni(OH)_2$, and SeO_2 (a total of 1.5 g; Sigma-Aldrich product materials) with a molar ratio of 2:1:3 were dissolved in deionized water. The solution was stirred continuously in the air until it became homogeneous. Then it was transferred into a stainless-steel Teflon autoclave (capacity ~125 mL; filling ~80%). The autoclave was then sealed and placed in a furnace. The sealed autoclave was slowly heated up to 230 °C for 20 h. Further, the furnace temperature of 230 °C was held for 200 h and then cooled to 150 °C at a rate of 1 °C/h. Finally, the autoclave was cooled down to room temperature. The obtained products were collected, purified with distilled water, and dried in the air at room temperature. As a result, golden yellow single crystals of $Sr_2Ni(SeO_3)_3$ with dimensions of 1×1 mm^2 were obtained, as shown in the inset of Fig. 2.

Synchrotron x-ray powder diffraction (SXRD) experiments were conducted for phase identification and structure analysis. The SXRD patterns were obtained with the MYTHEN detector with a 20-keV beam at beamline 19A, Taiwan Photon Source (TPS), National Synchrotron Radiation Research Center in Taiwan. The powder sample was packed in a borosilicate capillary that was kept spinning during data collection. The collected patterns were analyzed with the Rietveld method using the program Bruker DIFFRAC.TOPAS. Further, powder x-ray diffraction was employed to identify the crystal plane of the as-grown crystal using D8. The magnetic susceptibilities and magnetization measurements were carried out with a

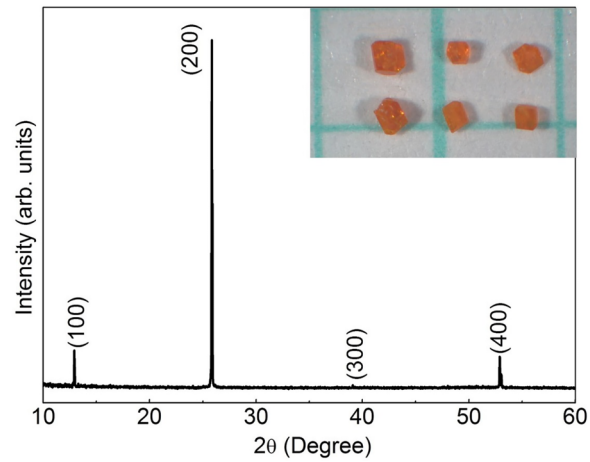

FIG. 2. X-ray diffraction pattern of $Sr_2Ni(SeO_3)_3$ single crystals measured at room temperature. The inset shows a photographic image of as-grown single-crystal morphology.

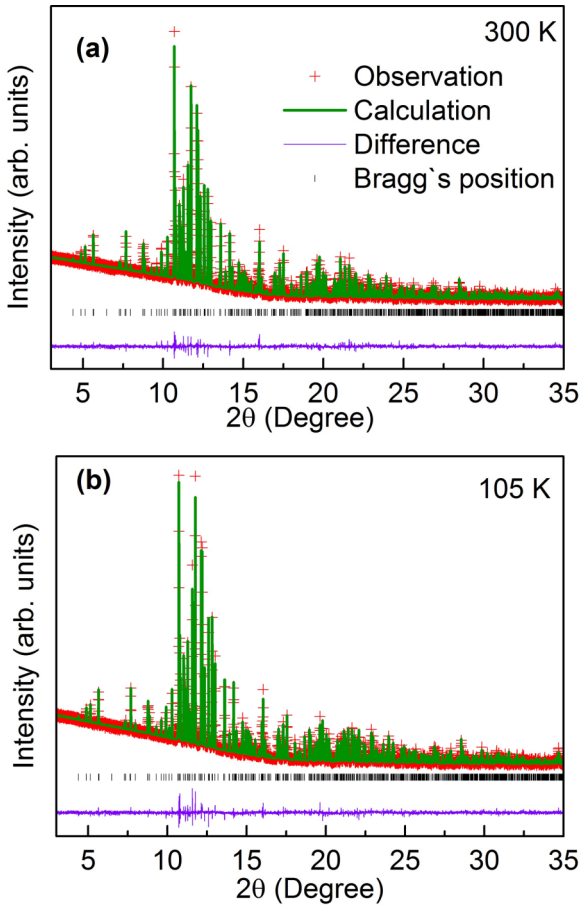

FIG. 3. Synchrotron x-ray powder diffraction (SXRD) patterns of pulverized single crystals of $Sr_2Ni(SeO_3)_3$ at (a) $T = 300$ K and (b) $T = 105$ K. The observed, calculated, and difference patterns are denoted by the red crosses and green and purple lines, respectively. The diffraction peaks are marked with black lines at the bottom of the figures.

Quantum Design vibrating sample magnetometer. The specific heat capacity of a single crystal was measured with a Physical Properties Measurement System (PPMS-Quantum Design).

To gain further insights into the electronic and magnetic properties of the compound, we performed DFT calculations with the generalized gradient approximation (GGA). To give a proper description of the electron-electron correlations associated with the $3d$ electrons of the Ni atom, we applied the GGA + U method with $U_{\text{eff}} = U - J = 6.0$ eV [11–13]. We used the projector augmented-wave method implemented in VASP [14–16]. The wave functions were expanded on a plane-wave basis with an energy cutoff of 520 eV. The Brillouin zone integration was performed with a Γ-centered Monkhorst-Pack k-point mesh of $6 \times 4 \times 2$. The structure was relaxed for both the lattice constants and the atomic positions until atomic forces on each atom converged to within 0.01 eV/Å. The self-consistent total energies converged up to 10^{-4} eV. For the density of states (DOS) calculations, we used the tetrahedron integration method with Blöchl corrections. The extracted exchange parameters are discussed in Sec. III D.

III. RESULTS

A. Crystal structure

The plane of single crystals was examined by an x-ray diffraction pattern, as displayed in Fig. 2. The grown crystal reveals a diffraction (h00) crystal plane. The SXRD pattern of single-crystal powder of the $Sr_2Ni(SeO_3)_3$ sample was collected at $T = 300$ and 105 K with a high-resolution diffractometer at beamline TPS 19A. The pattern was analyzed with the Rietveld method. The refinement result is presented in Fig. 3, and the refinement parameters are listed in Tables I and II. Overall, these findings demonstrate that the $Sr_2Ni(SeO_3)_3$ sample is of high quality and crystallizes in triclinic symmetry with the $P\bar{1}$ space group. The refined lattice parameters

TABLE I. Refinement parameters and atomic coordinates obtained from Rietveld refinement results of $T = 300$ K SXRD patterns of single-crystal powder of $Sr_2Ni(SeO_3)_3$. Space group = $P\bar{1}$ (No. 2) $a = 7.28735(3)$ Å, $b = 7.58525(3)$ Å, and $c = 8.72579(4)$ Å; $\alpha = 103.0281(2)°$, $\beta = 105.5858(2)°$, and $\gamma = 95.2485(2)°$; $V = 446.655(3)$ Å^3, $R_{wp} = 1.65\%$, $R_p = 1.20\%$, and goodness of fit (GOF)= 2.70.

Atom	Site	x	y	z	B_{eq}/A^2
Sr1	2i	0.2437(4)	0.0867(4)	0.3894(4)	0.82(8)
Sr2	2i	0.3687(4)	0.5169(4)	0.1930(4)	0.77(9)
Ni1	2i	0.9072(6)	0.6656(5)	0.2527(5)	1.3(1)
Se1	2i	0.6369(4)	0.9172(4)	0.2021(4)	1.3(1)
Se2	2i	0.9037(5)	0.2119(4)	0.0452(4)	0.85(9)
Se3	2i	0.7685(5)	0.3621(4)	0.4113(4)	1.03(8)
O1	2i	0.494(2)	0.872(2)	0.321(2)	1.0(1)
O2	2i	0.852(2)	0.924(2)	0.355(2)	
O3	2i	0.634(2)	0.691(2)	0.092(2)	
O4	2i	0.106(2)	0.227(2)	0.176(2)	
O5	2i	0.832(2)	0.429(2)	0.071(2)	
O6	2i	0.933(2)	0.190(2)	0.858(2)	
O7	2i	0.524(2)	0.270(2)	0.339(2)	
O8	2i	0.769(2)	0.594(2)	0.400(2)	
O9	2i	0.802(2)	0.362(2)	0.602(2)	

TABLE II. Refinement parameters and atomic coordinates obtained from Rietveld refinement results of $T = 105$ K SXRD patterns of single-crystal powder of $Sr_2Ni(SeO_3)_3$. Space group = $P\bar{1}$ (No. 2) $a = 7.27156(3)$ Å, $b = 7.57129(3)$ Å, and $c = 8.69854(3)$ Å; $\alpha = 103.0220(2)°$, $\beta = 105.5400(2)°$, and $\gamma = 95.2344(2)°$; $V = 443.626(3)$ Å^3, $R_{wp} = 1.67\%$, $R_p = 1.20\%$, goodness of fit (GOF) = 2.76.

Atom	Site	x	y	z	B_{eq}/A^2
Sr1	2*i*	0.2437(4)	0.0884(4)	0.3903(3)	0.76(8)
Sr2	2*i*	0.3722(4)	0.5179(3)	0.1933(3)	0.38(8)
Ni1	2*i*	0.9121(5)	0.6666(5)	0.2499(4)	0.5(1)
Se1	2*i*	0.6370(4)	0.9187(4)	0.2040(3)	0.45(8)
Se2	2*i*	0.9026(4)	0.2121(4)	0.0438(3)	0.29(8)
Se3	2*i*	0.7676(4)	0.3623(4)	0.4117(4)	0.65(8)
O1	2*i*	0.507(2)	0.883(2)	0.328(2)	0.5(1)
O2	2*i*	0.849(2)	0.942(2)	0.346(2)	
O3	2*i*	0.638(2)	0.703(2)	0.089(2)	
O4	2*i*	0.125(2)	0.239(2)	0.177(2)	
O5	2*i*	0.817(2)	0.425(2)	0.080(2)	
O6	2*i*	0.927(2)	0.199(2)	0.863(2)	
O7	2*i*	0.538(2)	0.298(2)	0.357(2)	
O8	2*i*	0.788(2)	0.581(2)	0.404(2)	
O9	2*i*	0.819(2)	0.360(2)	0.607(2)	

at room temperature are consistent with previously reported results [10]. Furthermore, thermal contraction was measured from 300 to 105 K, and no structural transition was observed in the measured temperature range.

B. Magnetic susceptibility and magnetization

Figure 4 shows the temperature dependence of dc magnetic susceptibility $\chi(T) = M(T)/H$ for a single crystal of $Sr_2Ni(SeO_3)_3$ measured under an external magnetic field of 100 Oe applied parallel and perpendicular to the a axis. The $\chi(T)$ data increase with decreasing temperature and then reach a maximum centered at $T^{\chi}_{max} \sim 7.8$ K. This broad feature in $\chi(T)$ is typical for low-dimensional magnetic systems and is associated with the onset of short-range spin ordering or the formation of a spin gap [17,18]. As can be seen in the inset of Fig. 4(a), with decreasing temperature below T^{χ}_{max}, $\chi(T)$ decreases down to 2 K for $H \perp a$. A kink feature is discernible around $T_N \sim 3.4$ K. As evident from the sharp peak in $d\chi/dT$, this anomaly corresponds to a 3D AFM transition. In contrast to $H \perp a$, $\chi(T)$ becomes flat below T_N, indicating that the magnetic hard axis is along the (100) direction.

Further, we find no splitting of $\chi(T)$ between the zero-field-cooled (ZFC) and field-cooled (FC) cycles in the temperature range of $T = 2$–300 K for $H \perp a$, while a small splitting at $T < 2.5$ K is observed between the ZFC and FC cycles for $H \parallel a$ [see the inset of Fig. 4(a)]. A small divergence at $T < 20$ K in $\chi(T)$ is appreciable between $H \perp a$ and $H \parallel a$, indicating the presence of small anisotropy due to the weak spin-orbit coupling of Ni^{2+} ions.

For a quantitative analysis of $\chi(T)$, the inverse magnetic susceptibility vs T plot in Fig. 4(b) reveals two linear regimes: $T = 300$–170 K (designated as HT) and 160–20 K (LT) in both directions. This observation suggests that a change in exchange interactions occurs at ~160 K. Since our SXRD data exclude the possibility of a structural transition, local lattice distortions may be responsible for modulating superexchange paths.

Using the Curie-Weiss (CW) law $\chi(T) = C/(T - \theta_{CW})$, we analyze the $\chi(T)$ data in two linear regimes. The deduced parameters are tabulated in Table III. The effective magnetic moment μ_{eff} estimated from the CW constant is in reasonable agreement with the theoretical spin-only value of 2.83 μ_B for Ni^{2+} ($S = 1$, $g = 2$). On the other hand, the CW temperature changes its sign from positive to negative in the HT and LT

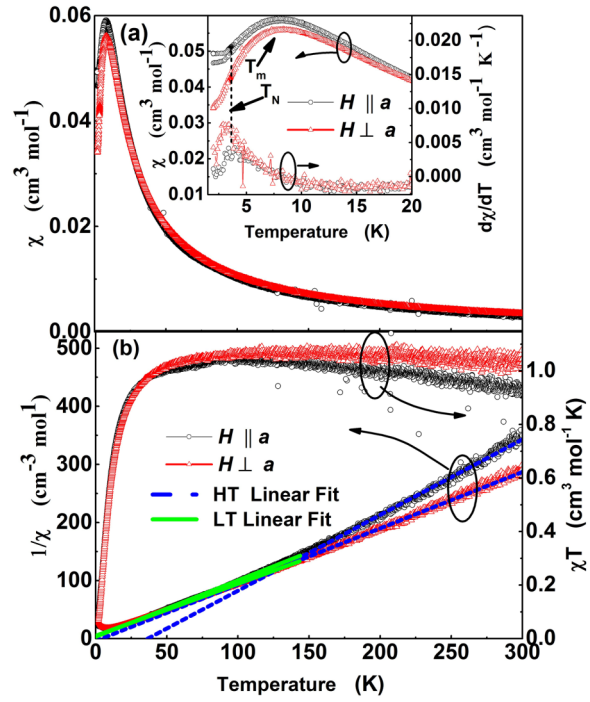

FIG. 4. (a) Magnetic susceptibility $\chi(T)$ of $Sr_2Ni(SeO_3)_3$ single crystal as a function of temperature measured at $H = 100$ Oe for $H \parallel a$ and $H \perp a$. The inset zooms in the low-temperature $\chi(T)$ vs T (left axis) and $d\chi/dT$ vs T (right axis). (b) Temperature dependence of the inverse magnetic susceptibility $1/\chi$ (left axis) and χT (right axis). The solid and dashed lines correspond to linear fits in the low-T and high-T regimes, respectively.

TABLE III. The magnetic parameters deduced from the CW law fit of the inverse magnetic susceptibility.

	CW law fitting temperature regime					
	300–170 K			160–20 K		
Single-crystal direction	C (emu K/mol)	μ_{eff} (μ_B)	θ_{CW} (K)	C (emu K/mol)	μ_{eff} (μ_B)	θ_{CW} (K)
$H \parallel a$	1.031	2.87	4.16	1.100	2.96	−4.45
$H \perp a$	0.768	2.48	36.61	1.032	2.87	−3.47

regions, respectively. This alludes to the fact that the dominant exchange interactions between Ni^{2+} ions are ferromagnetic (FM) in the HT regime, while switching to AFM interactions in the LT regime. Further, we plot the product of magnetic susceptibility and temperature $\chi(T)^*T$ vs T in Fig. 4(b). The nonmonotonic decrease of $\chi(T)^*T$ with decreasing temperature, incompatible with a monotonic decrease of $\chi(T)^*T$ for AFM systems, lends further support for the change of dominant exchange interactions. As a ground state is dictated by LT magnetic behavior, based on the $\chi(T)$ analysis, we infer that the AFM intrachain exchange interaction between Ni^{2+} ions gives rise to a short-range magnetic correlation at $T_m \sim 7.8$ K. Eventually, weak interchain AFM interactions lead to a 3D AFM ordering at $T_N \sim 3.4$ K.

Figure 5 shows the temperature and field dependence of $\chi(T, H)$ for $H \parallel a$ and $H \perp a$. As a magnetic field increases, the magnitude of $\chi(T)$ increases continuously, implying a field-induced partial polarization of the magnetic moment. Additionally, both T_N and T_{max} shift to lower temperatures,

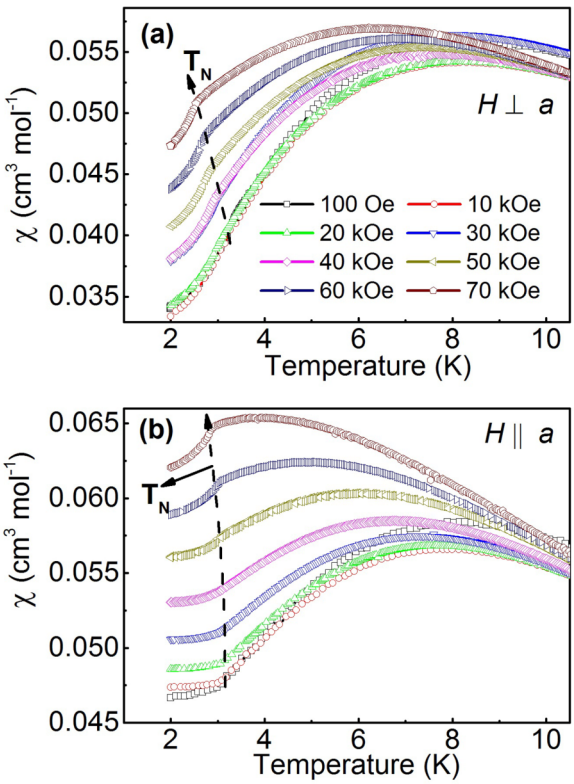

FIG. 5. Temperature and field dependence of the magnetic susceptibility under a different magnetic field applied along the (a) $H \perp a$ and (b) $H \parallel a$ directions.

suggesting that the applied field suppresses AFM correlations and ordering. On the application of a magnetic field, the suppression of T_N by applying magnetic fields is typical for conventional AFM materials [19,20]. It is worth noting that the effect of the magnetic field is different for the two field orientations. The enhancement of $\chi(T)$ and the shift of T_{max} are more pronounced for $H \parallel a$ than $H \perp a$. Conversely, the reduction of T_N is stronger for $H \perp a$ than $H \parallel a$. These observations suggest that the magnetic field has a somewhat anisotropic effect on the material.

Figure 6(a) displays the magnetization curves $M(H)$ measured at 2 K for fields parallel and perpendicular to the a axis. In both directions, the $M(H)$ curves exhibit nonlinear behavior as a convex shape. The lack of peaklike features in dM/dT rules out the occurrence of spin-flop transitions. To reach full saturation magnetization $M_s = 2gS\mu_B \approx 2\ \mu_B$, high-field magnetization measurements were performed up to 130 kOe. The magnetization shows an S-shaped curvature, characteristic of 1D spin systems. However, a half-step magnetization plateau, expected for $S = 1$ bond alternating spin chains, could not be identified [21]. Instead, we observe hysteric behavior in the field range between 62 and 82 kOe, suggesting a field-induced first-order transition or crossover. We speculate that the competition between spin-ion anisotropy and interchain interactions smears out the half-magnetization plateau and induces exotic magnetic phases around the half-magnetization plateau regime, warranting future investigation.

C. Specific heat

Figure 7(a) shows the temperature dependence of the specific heat $C_P(T)$ for the $Sr_2Ni(SeO_3)_3$ sample, which was measured in the $T = 2$–90 K range at zero magnetic fields. Evident from an enlarged view of $C_P(T)$ in Fig. 7(b), C_P reveals a broad maximum at $T_{\text{max}}^{C_P} \sim 6.3$ K and a λ-type anomaly at 3.1 K, confirming the long-range AFM ordering. Noteworthy is that $T_{\text{max}}^{C_P}$ found in the $C_P(T)$ data is somewhat lower than the onset temperature of short-range ordering $T_{\text{max}}^{\chi} \sim 7.8$ K determined by the $\chi(H = 100\ \text{Oe}, T)$ data. Such a discrepancy is commonly seen in low-dimensional magnetic systems [22–24].

Generically, the total specific heat C_P is comprised of three components: electronic, magnetic, and phonon terms. Due to the insulating nature of the $Sr_2Ni(SeO_3)_3$ compound, the electronic contribution can be assumed to be zero. Here, C_P can now be expressed as the sum of phonon (C_{ph}) and magnetic (C_{mag}) contributions $C_P = C_{\text{ph}} + C_{\text{mag}}$. Usually, the nonmagnetic isostructural compound gives the appropriate estimation of C_{ph}. Since the nonmagnetic isostructural compound is not available, the phonon contribution is estimated

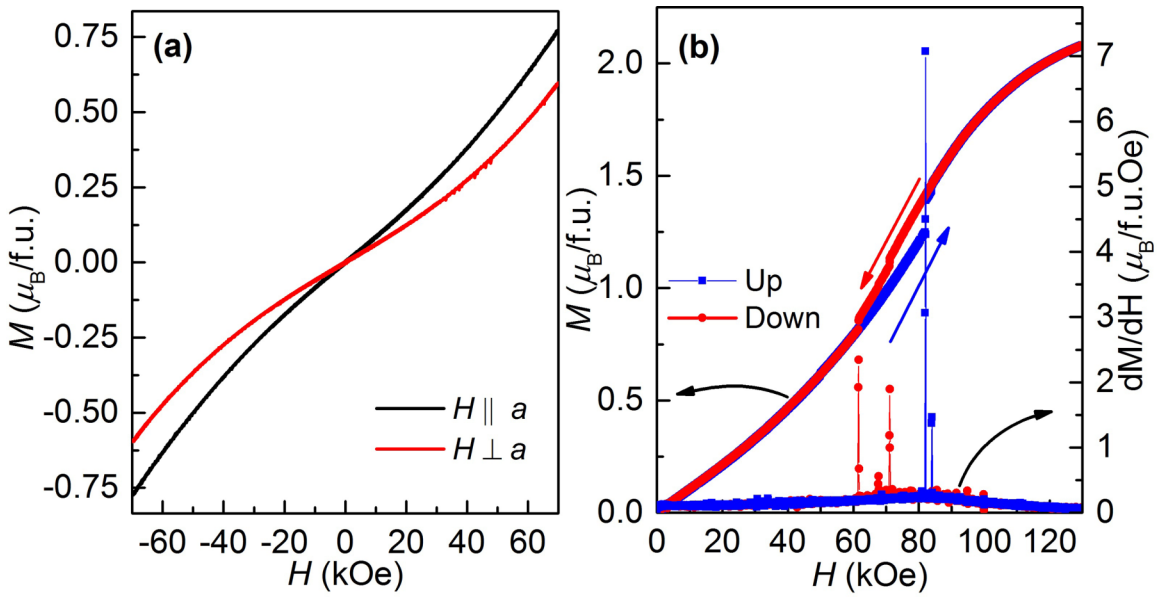

FIG. 6. (a) Magnetization of $Sr_2Ni(SeO_3)_3$ single crystal vs field measured for $H \parallel a$ and $H \perp a$ at 2 K. (b) (left axis) Magnetization vs magnetic field for single-crystal powder measured at 2 K up to 130 kOe and its derivative on the right axis (dM/dT vs H).

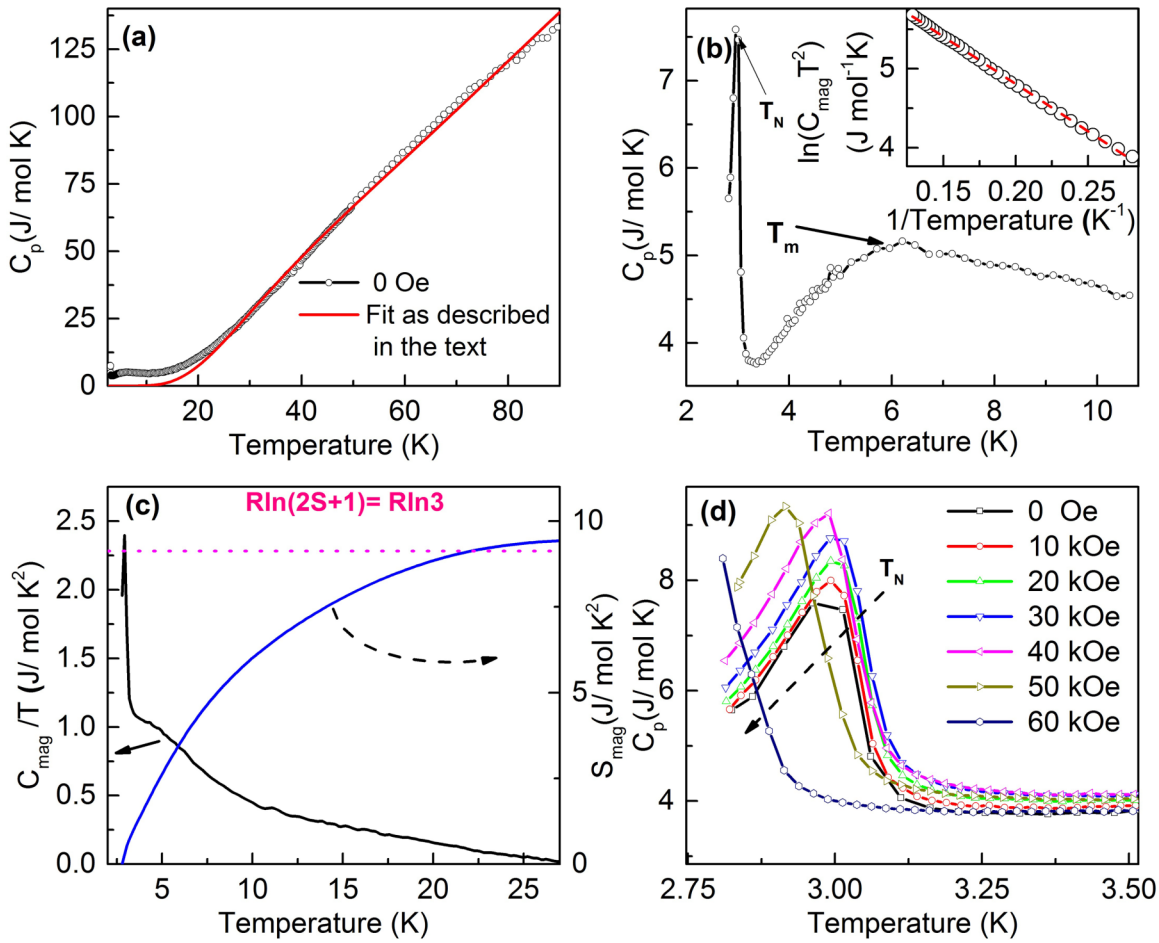

FIG. 7. (a) Specific heat capacity (C_P) data of $Sr_2Ni(SeO_3)_3$ single crystal at zero magnetic field and (b) an enlarged view at low temperatures. The inset shows a fit to the equation $C_{mag} = \tilde{n}R(\Delta/T)^2 e^{-\Delta/T}$. (c) Magnetic specific heat divided by temperature C_{mag}/T vs temperature (left axis) and their corresponding magnetic entropy S_{mag} (right axis). (d) Temperature and field dependence of the C_P data.

by the combination of Debye (acoustic modes) and Einstein (optical modes) models as [25]

$$C_{\rm ph} = kC_D + (1-k)C_E,$$
$$C_D = 9nR\left(\frac{T}{\theta_D}\right)^3 \int_0^{\theta_D/T} \frac{x^4 e^x}{(e^x-1)^2} dx,$$
$$C_E = 3nR\left(\frac{\theta_E}{T}\right)^2 \frac{e^{\theta_E/T}}{\left(e^{\theta_E/T}-1\right)^2},$$

where $x = \frac{\hbar\omega}{k_B T}$ and $n = 15$ is the total number of atoms, R is the molar gas constant, θ_D is the Debye temperature, and θ_E is the Einstein temperature. Here, k represents the weight percentage of $C_{\rm ph}$ to the $C_{\rm P}$ given by the Debye term. The $C_{\rm P}$ data measured at zero fields were fitted by the above expression in the $T = 20$–90 K range and were further extrapolated to 2 K. The obtained parameters are $\theta_D = 584 \pm 3$ K, $\theta_E = 125 \pm 5$ K, and $k = 0.77$. Then the estimated phonon contribution was subtracted from the measured $C_{\rm P}$ data to determine the magnetic contribution ($C_{\rm mag}$) to the specific heat. Finally, the magnetic entropy was calculated using the relation $S_{\rm m}(T) = \int C_{\rm mag}/T \, dT$ and is shown in Fig. 7(c) (right axis). As the temperature approaches 27 K, S_m saturates with an approaching value ~9.4 (J/mol K), which is fairly close to the expected value $R\ln(2S+1) \approx 9.13$ J/(mol K) from mean-field theory for $S = 1$. The entropy release of 0.4 J/mol K at $T_{\rm N}$ amounts to ~4.26% of the saturation value. The rest 95.74% of S_m is released at high temperatures above $T_{\rm N}$, lending further support that low-dimensional magnetic correlations persist well above $T_{\rm N}$ [18,26]. As shown in the inset of Fig. 7(b), the low-T $C_{\rm mag}$ data are fitted by the expression $C_{\rm mag} = \tilde{n}R(\Delta/T)^2 e^{-\Delta/T}$, where $\tilde{n}$ is the number of excited states per spin dimer. The best fit at low Ts yields an energy gap $\Delta = 12$ K. This energy scale roughly doubles $T_{\rm max}^{C_{\rm P}}$ and $T_{\rm max}$. This unphysical value of Δ negates the development of spin-dimer-like correlations. Noteworthy is that the $J_{\rm eff} = \frac{1}{2}$ counterpart $Sr_2Co(SeO_3)_3$, forming a coupled alternating chain system, has a spin-singlet ground state of $\Delta \approx 3$ K [27]. Given the fact that both $Sr_2Co(SeO_3)_3$ and $Sr_2Ni(SeO_3)_3$ compounds feature substantial bond alternation, the occurrence of long-range magnetic order in the latter is attributed to single-ion anisotropy and enhanced 3D interchain interactions.

In addition, we measured $C_{\rm P}(T, H)$ in various magnetic fields in the temperature range between 2.7 and 4 K to trace the AFM transition temperature with field. As shown in Fig. 7(d), $T_{\rm N}$ shifts to a lower temperature. Interestingly, a significant increment in $C_{\rm P}(T, H)$ is observed at $T_{\rm N}$ with increasing magnetic field, which is at odds with a second-order phase transition. Notably, this signature contrasts with the reduction in the magnitude of $C_{\rm P}(T_{\rm N}, H)$ typically observed for AFM systems, including low-dimensional and frustrated magnetic compounds.

D. Theoretical calculations

Starting from the experimentally determined lattice parameters $a = 7.2873$ Å, $b = 7.5852$ Å, and $c = 8.7258$ Å and 2 f.u. per unit cell, we performed structural optimization for both FM and AFM configurations. We find that the AFM configuration has lower energy (see Table IV) with optimized lattice parameters $a = 7.4189$ Å, $b = 7.7617$ Å, and $c = 8.8376$ Å, being in close agreement with the experiment. The magnetic moment of Ni ions is calculated as 1.78 $\mu_{\rm B}$/atom, which is ~15% smaller than the experimental value of 2.1 $\mu_{\rm B}$/atom. This may be because DFT-based calculations usually underestimate the moment size for $3d$ transition metals by transferring some spin densities onto the surrounding O^{2-} ions. However, if we add the magnetic moments of all atoms in the unit cell, a total value of 3.82 $\mu_{\rm B}$ can be obtained and corresponds to a moment of 1.91 $\mu_{\rm B}$ per Ni ion, which is much closer to the experimental value.

TABLE IV. Calculated total energy, ΔE relative to the total energy of the FM state ($E_{\rm FM} = -170.6345$ eV/f.u.), and magnetic moment of the Ni atom ($m_s^{\rm Ni}$ $\mu_{\rm B}$/atom).

Configuration	ΔE (meV/f.u.)	$m_s^{\rm Ni}$ ($\mu_{\rm B}$/atom)
FM	0.0	1.78
AFM1	−1.15	1.78
AFM2	−0.40	1.78

The calculated electronic band structure and DOS are displayed in Figs. 8(a) and 8(b), respectively. From the band structure, the material is an insulator with a band gap of ~3.77 eV. Analysis of site-resolved DOS reveals that the valence band located at −0.15 eV is due to the O p, Se p, and Ni d states. The valence band width below −0.15 eV is

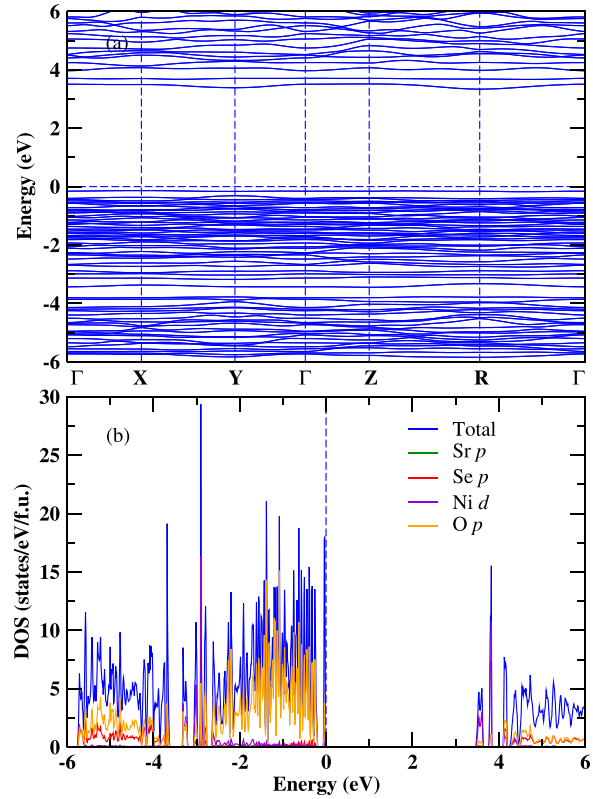

FIG. 8. (a) Calculated electronic band structure and (b) density of states (DOS) of $Sr_2Ni(SeO_3)_3$. The top of the valence band is set to zero.

~3 eV, and the bands are due to hybridization between the O p, Ni d, and Se p states with more weights of O p states. However, the bands below −3.6 eV are dominated by Ni d states with significant contributions from the O p and Se p states. This indicates that covalent bondings are dominant in this material. The conduction band is mainly dominated by the Ni d states. Therefore, $Sr_2Ni(SeO_3)_3$ can be classified as a charge-transfer insulator due to the interaction between the O p and Ni d states that leads to the band gap.

Further, to understand the magnetic behavior of $Sr_2Ni(SeO_3)_3$, we calculated the exchange-interaction parameters (J_{ij}) between neighboring Ni atoms located at different distances from one another. We constructed a supercell that consists of 6 Ni atoms and carried out the calculations for three different magnetic configurations. The calculated total energies and the magnetic moments are presented in Table IV. As can be seen from Table IV, the AFM1 structure has the lowest energy and thus becomes the magnetic ground state of $Sr_2Ni(SeO_3)_3$. To figure out the nature and magnitude of exchange-interaction parameters, we use a Heisenberg model. The Heisenberg Hamiltonian can be expressed as $H = E_0 - \Sigma_{i,j} J_{ij} S_i S_j$, where E_0 is the total energy for all the spin-independent interactions, J_{ij} are the exchange-interaction parameters between the Ni atoms at sites i and j, and S_i and S_j are the unit vectors representing the directions of the local magnetic moments at sites i and j, respectively. By solving the set of equations, we find the values of J_{ij}. With $U_{\text{eff}} = 3$ eV, the intrachain couplings J_{i1} and J_{i2} at distances of 5.1394 and 5.3997 Å in the bc plane are calculated to be −4.99 and 0.34 K, respectively. The J_{i1} and J_{i2} interactions are due to the Ni-O-Se-O-Ni path where Ni has octahedral coordination and Se has triangular nonplanar coordination with O atoms. The interchain interactions are estimated to be $J_{c3} = -1.80$ K and $J_{c4} = -0.19$ K. The other exchange interactions are negligibly small. By using the calculated exchange-coupling constants, the CW temperature is evaluated to be $\theta_{\text{CW}} = -4.42$ K, which is in good accord with the experimental value. Contrary to the structural spin chain, our DFT calculations show that $Sr_2Ni(SeO_3)_3$ can be approximated as the J_{i1}-J_{c3} alternating spin chain.

IV. DISCUSSION AND CONCLUSIONS

Based on the $\chi(T, H)$ and $C_P(T, H)$ data, we construct a H-T phase diagram. As can be seen in Fig. 9, $Sr_2Ni(SeO_3)_3$ features three states: high-T paramagnetic state, short-range order (SRO), and AFM-ordered state. Overall, T_N and T_m shift to lower temperatures with increasing H. However, a close look reveals that, for $H \parallel a$, the SRO phase evolves in a nonmonotonic way: With increasing field, T_m shifts initially to a higher temperature and then moves toward a lower temperature. This may be associated with the competing effect of single-ion anisotropy (not considered in DFT calculations) and Heisenberg interaction. To draw a H-T phase boundary of T_N all the way down to zero temperature, we employ the empirical formula $H = H_0\,(1-T/T_N)^{0.5}$, where H_0 is the critical magnetic field. The extrapolated critical field is $H_0 = 96$ and 142 kOe for $H \perp a$ and $H \parallel a$, respectively. As to the orientation dependence of H_0, the smaller critical field for $H \perp a$ than $H \parallel a$ is consistent with the fact that $H \perp a$ is the magnetic easy axis.

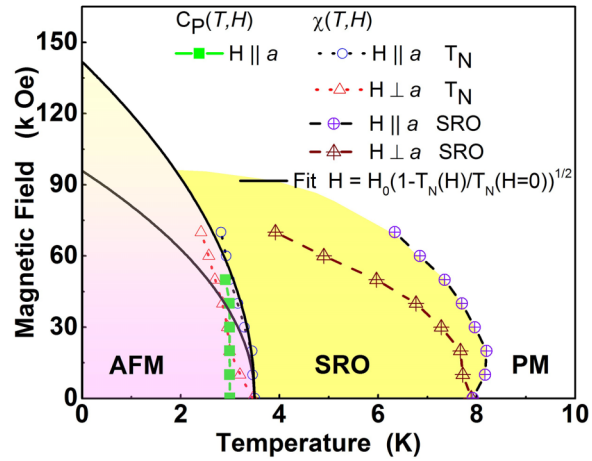

FIG. 9. H-T phase diagram constructed from $\chi(T, H)$ and $C_P(T, H)$ for $Sr_2Ni(SeO_3)_3$. The solid black curves are fits of the H-T phase boundary to the expression $H = H_0[1–T_N(H)/T_N(H = 0)]^{1/2}$.

To summarize, we have successfully grown high-quality single crystals of $Sr_2Ni(SeO_3)_3$ and characterized their structural, magnetic, and thermodynamic properties. Our magnetic susceptibility and specific heat results unambiguously identify the onset of AFM ordering at $T_N \sim 3.3$ K and a short-range magnetic order at $T_m \sim 7.8$ K. The magnetic entropy involved at T_N amounts to only 4.26% of the total S_m, and the remaining 95.74% entropy is released at high temperatures up to $8T_N$, indicative of the significance of low-dimensional spin fluctuations. The magnetization curve shows hysteric behavior around the half-magnetization plateau predicted for alternating $S = 1$ spin chains. The broad maximum value in $C_{\text{mag}}/R \sim 0.6$ accords with the theoretical calculation for a $S = 1$ AFM chain. Based on our observations, we conclude that the studied compound can be considered as coupled alternating $S = 1$ spin chains, which are located in an AFM ordered phase. Further, we construct a field-temperature phase diagram, which reveals a nonmonotonic phase boundary of T_m for an external field applied along a hard axis. This signals the competing effects of single-ion anisotropy and Heisenberg interactions, calling for future investigations to set up an effective spin Hamiltonian including magnetic anisotropy as well as to clarify the presence of spin-singlet correlations.

ACKNOWLEDGMENTS

I.P.M. thanks the Department of Science and Technology in India for financial support through INSPIRE faculty Award No. DST/INSPIRE/04/2016/002275(IFA16-PH171) and Banaras Hindu University for Institutes of Eminence (IoE) Seed Grant. K.S. acknowledges the financial assistance from the University Grants Commission, India, for D. S. Kothari Post-Doctoral Fellowship Award No. F.4-2/2006 (BSR)/PH/18-19/0099. R.S. acknowledges the financial support provided by the Ministry of Science and Technology in Taiwan under Projects No. NSCT-111-2124-M-001-009;

No. NSCT-110-2112-M-001-065-MY3 and No. AS-iMATE-111-12. The work at SKKU was supported by the National Research Foundation of Korea (Grants No. 2020R1A2C3012367 and No. 2020R1A5A1016518).

[1] I. Affleck, J. Phys.: Condens. Matter. **1**, 3047 (1989).
[2] C. Yasuda, S. Todo, K. Hukushima, F. Alet, M. Keller, M. Troyer, and H. Takayama, Phys. Rev. Lett. **94**, 217201 (2005).
[3] H. J. Schulz, Phys. Rev. Lett. **77**, 2790 (1996).
[4] F. D. M. Haldane, Phys. Rev. Lett. **50**, 1153 (1983).
[5] F. D. M. Haldane, Phys. Lett. A **93**, 464 (1983).
[6] A. Zheludev, T. Masuda, I. Tsukada, Y. Uchiyama, K. Uchinokura, P. Böni, and S.-H. Lee, Phys. Rev. B **62**, 8921 (2000).
[7] D. C. Dender, D. Davidović, D. H. Reich, C. Broholm, K. Lefmann, and G. Aeppli, Phys. Rev. B **53**, 2583 (1996).
[8] T. Sakai and M. Takahashi, Phys. Rev. B **42**, 4537 (1990).
[9] Y. Kato and A. Tanaka, J. Phys. Soc. Japan **63**, 1277 (1994).
[10] P. S. Berdonosov, K. A. Batunin, A. V. Olenev, and V. A. Dolgikh, Russ. J. Inorg. Chem. **55**, 6 (2010).
[11] J. P. Perdew, K. Burke, and M. Ernzerhof, Phys. Rev. Lett. **77**, 3865 (1996).
[12] S. L. Dudarev, G. A. Botton, S. Y. Savrasov, C. J. Humphreys, and A. P. Sutton, Phys. Rev. B **57**, 1505 (1998).
[13] M. Petersen, J. Hafner, and M. Marsman, J. Phys.: Condens. Matter **18**, 7021 (2006).
[14] G. Kresse and J. Hafner, Phys. Rev. B **47**, 558 (1993); **49**, 14251 (1994).
[15] G. Kresse and J. Furthmüller, Comput. Mater. Sci. **6**, 15 (1996).
[16] G. Kresse and D. Joubert, Phys. Rev. B **59**, 1758 (1999).
[17] J. C. Bonner and M. E. Fisher, Phys. Rev. **135**, A640 (1964).
[18] I. P. Muthuselvam, R. Sankar, V. Nand Singh, G. Narsinga Rao, W. L. Lee, G. Y. Guo, and F. C. Chou, Inorg. Chem. **54**, 4303 (2015).
[19] I. P. Muthuselvam, R. Sankar, A. V. Ushakov, G. N. Rao, S. V. Streltsov, and F. C. Chou, Phys. Rev. B **90**, 174430 (2014).
[20] I. P. Muthuselvam, R. Nehru, K. Ramesh Babu, K. Saranya, S. N. Kaul, S.-M. Chen, W.-T. Chen, Y. Liu, G.-Y. Guo, F. Xiu *et al.*, J. Phys.: Condens. Matter. **31**, 285802 (2019).
[21] R. Sato, K. Kindo, Y. Narumi, and M. Hagiwara, J. Magn. Magn. Mater. **177–181**, 645 (1998).
[22] V. Gnezdilov, P. Lemmens, A. A. Zvyagin, V. O. Cheranovskii, K. Lamonova, Yu. G. Pashkevich, R. K. Kremer, and H. Berger, Phys. Rev. B **78**, 184407 (2008).
[23] H. T. Lu, Y. J. Wang, S. Qin, and T. Xiang, Phys. Rev. B **74**, 134425 (2006).
[24] E. F. Chagas, R. E. Rapp, D. E. Rodrigues, N. M. C. Casado, and R. Calvo, J. Phys. Chem. B **110**, 8052 (2006).
[25] I. P. Muthuselvam, K. Saranya, D. Kasinathan, R. N. Bhowmik, R. Sankar, N. Dhenadhayalan, G. J. Shu, W.-t. Chen, L. Kavitha, and K.-C. Lin, Phys. Rev. B **104**, 174442 (2021).
[26] L. J. de Jongh and A. R. Miedema, Adv. Phys. **23**, 1 (1974).
[27] I. P. Muthuselvam, R. Madhumathy, K. Saranya, K. Moovendaran, S. Lee, K.-Y. Choi, W.-t. Chen, C.-W. Wang, P.-J. Chen, M. Ponmurugan *et al.*, Phys. Rev. B **106**, 214417 (2022).